Rational Design of Mesoporous $CuO-CeO_2$ Catalysts for NH_3-SCR Applications Guided by Multiple *In Situ* Spectroscopies

Jun Shen[1], Stefan Lauterbach,[2] Christian Hess[1*]

[1]Eduard Zintl Institute of Inorganic and Physical Chemistry, TU Darmstadt, Alarich-Weiss-Str. 8, 64287 Darmstadt, Germany

[2]Institut für Angewandte Geowissenschaften, TU Darmstadt, Schnittspahnstr. 9, 64287 Darmstadt, Germany

*email: christian.hess@tu-darmstadt.de

Keywords

$CuO-CeO_2$, NH_3-SCR, rational design, mesoporous, impregnation, *in situ* mechanism

This document is the Accepted Manuscript version of a Published Work that appeared in final form in ACS Applied Materials & Interfaces, copyright © 2022 The Authors. Published by American Chemical Society after peer review and technical editing by the publisher. To access the final edited and published work see https://doi.org/10.1021/acsami.2c13367

Urheberrechtlich geschützt / In Copyright: https://rightsstatements.org/page/InC/1.0/

Graphical Abstract

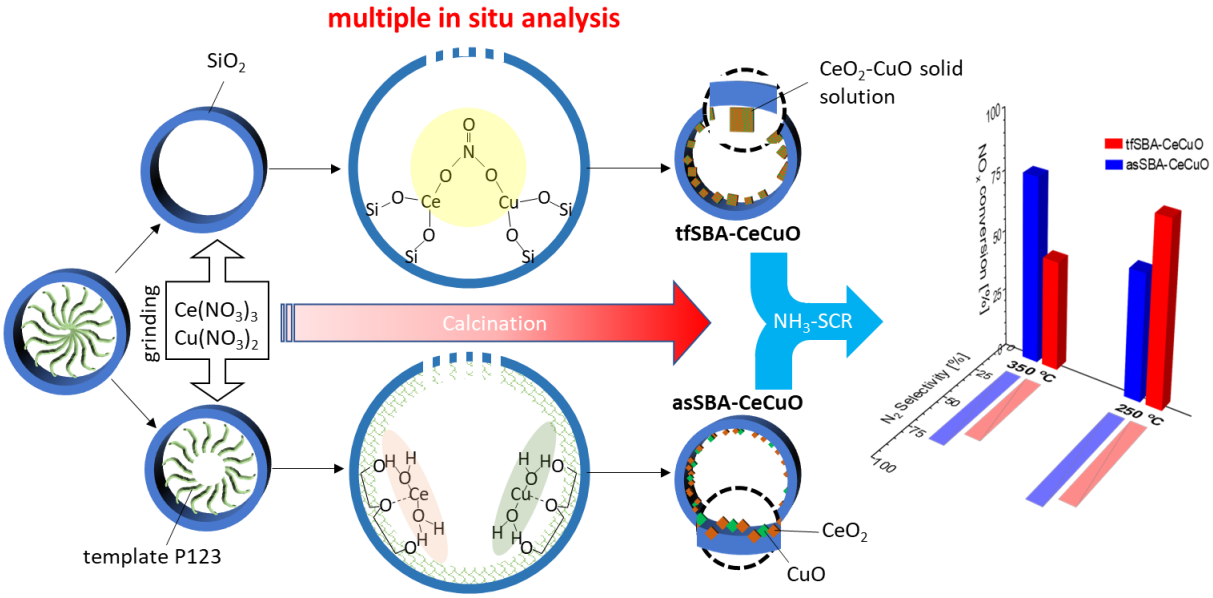

Abstract

Efficient non-toxic catalysts for low temperature NH_3-SCR applications are of great interest. Owing to their promising redox and low-temperature activity, we prepared CuO-CeO_2 catalysts on a mesoporous SBA-15 support by using targeted solid-state impregnation (SSI), guided by multiple *in situ* spectroscopy. The use of template P123 allowed dedicated modification of the surface properties of the SBA-15 matrix, resulting in a changed reactivity behavior of the metal precursors during the calcination process. To unravel the details of the transformation of the precursors to the final catalyst material, we applied *in situ* DRIFT, UV-Vis, and Raman spectroscopies as well as online FTIR monitoring of the gas-phase composition, besides *ex situ* surface, porosity, and structural analysis. The *in situ* analysis reveals two types of nitrate decomposition mechanisms: a nitrate bridging route leading to the formation of a CuO-CeO_2 solid solution with increased low-temperature NH_3-SCR activity, and a hydrolysis route, which facilitates the formation of binary oxides CuO+CeO_2 showing activity over a broader temperature window peaking at higher temperatures. Our findings demonstrate that a detailed understanding of catalytic performance requires a profound knowledge of the calcination step and that the use of *in situ* analysis facilitates the rational design of catalytic properties.

1. Introduction

Nitrogen oxides (NO_x) may cause environmental problems including photochemical smog and acid rain, while endangering the human health.[1] NH_3 selective catalytic reduction (NH_3-SCR) of NO is an effective NO_x removal technology that has been widely used in various fossil fuel industries, such as thermal power stations and automobiles.[2, 3] Prominent technical catalysts for this reaction are vanadia containing oxides (i.e., V_2O_5-WO_3/TiO_2) due to their high NO_x removal efficiency. However, their main drawbacks are the toxicity of vanadia and the narrow and high operation temperature window.[4] A variety of transition metal oxides, including MnO_x and Fe_2O_3,[5, 6] were reported as active catalysts for low temperature (LT) SCR reactions. However, their industrial application is hampered by their irreversible deactivation in the presence of SO_2 and H_2O. As an alternative candidate, ceria-based catalysts have been developed, showing good SCR catalytic performance and environmental resistance, owing to the high oxygen storage capacity and remarkable redox properties.[7]

As a typical characteristic of heterogeneous catalysts, the catalytic efficiency is strongly related to the number of active sites. Small (nanosized) ceria particles exhibiting high surface areas and resistance against high-temperature aggregation are therefore preferred. To this end, mesoporous silica materials, such as MCM-41 and SBA-15, represent ideal carriers for metal oxide catalysts due to their high surface area and porosity. Besides, the exposed Si-OH sites facilitate oxide particle deposition and stable dispersion by forming Si-O-M linkages.[8] Accordingly, SBA-15 has previously been used as support material in NH_3-SCR catalysts, e.g. CoO/SBA-15,[9] NiO/SBA-15,[10] Fe_2O_3/SBA-15,[11] and CeO_2/SBA-15.[12-13] To improve the dispersion of cerium within the porous silicate matrix, a one-pot method has been applied, which, however, changed the original structure of SBA-15,[12] whereas the use of the wet impregnation (WI) method leads to an uneven distribution of ceria outside/inside the pores and facile aggregation.[14] The solid-state impregnation (SSI) method has been shown to enhance the resistance against thermal aggregation during calcination by strengthening the

interaction between metal oxides and the silica support.[15-16] In this context, a template P123 assisted SSI method was proposed, which leaves the surfactant template within the SBA-15 matrix during synthesis, forming a confined space for oxide growth. Applying this approach to the preparation of CeO_2/SBA-15, CuO/SBA-15, Ag-CeO_2/SBA-15, and NiO/SBA-15 materials has been shown to improve the catalytic performance.[17-20]

However, due to the overall poor NH_3-SCR reactivity of CeO_2-only catalysts,[21] we added copper oxide to form CuO-CeO_2/SBA-15 binary oxide catalysts, which are expected to improve the NH_3-SCR performance due to the synergetic effect through the redox equilibrium $Ce^{3+}+Cu^{2+} \leftrightarrow Ce^{4+}+Cu^{+}$.[22] In our previous work, we adopted the P123-assisted solid-state impregnation method to prepare CeO_2/SBA-15 materials and used *in situ* spectroscopy to elucidate the role of P123 in the loading of CeO_2 on SBA-15 including a physically formed confined space for growth of nano-oxides and chemically catalyzing the decomposition of active precursor.[23] To the best of our knowledge, this was the first time to use *in situ* spectroscopy to characterize the solid synthesis process of oxides supported on mesoporous materials. Based on the understanding of the synthesis mechanism, we are now able to design the template-assisted SSI method for the preparation of more relevant CeO_2-CuO catalysts for NH_3-SCR applications. Compared with the preparation of CeO_2/SBA-15, for the common situation of a co-loaded system the role of the template needs to be evaluated, as not only the dispersion but also the distribution of the two oxides needs to be taken into account. Thus, clarifying the chemical reaction processes occurring during the loading and formation of the final catalyst is of great importance for a controllable synthesis of bimetallic oxides and more complex oxides.

For the synthesis of metal oxide catalysts for SCR reactions, mainly two approaches are applied: (i) direct condensation from a metal precursor, or (ii) exchange with another coordination ligand, followed by condensation as metal oxide. Both routes involve the thermal decomposition of metal compounds and form the final oxide products at high temperature

calcination. For the SSI method applied here, the cerium and copper nitrate precursors are mixed with the support (SBA-15), followed by a calcination step, which includes the metal ion immigration to the pores and their interaction with support surface, the decomposition of the metal precursor, and the nucleation and growth of metal oxides. Due to the large number of processes occurring, calcination has often been considered as a 'black-box`.

In situ analysis is essential to elucidate the mechanisms of these processes, but it has proved difficult to use standard analytical techniques (e.g. TGA/DTA) for direct monitoring. To this end, the use of optical spectroscopy is of great interest, allowing a continuous data collection from outside the furnace (reaction) chamber, not affecting the calcination process. Applying *in situ* X-ray spectroscopy applied to nanomaterial synthesis has previously been shown to allow a description of the direct structural phase transformation.[24, 25] For a detailed understanding of the processes underlying synthesis, also the use of other techniques would be highly desirable, such as Raman spectroscopy, which probes the extended structure via phonons but also the short-range structure of solids, DRIFT spectroscopy, providing information on surface and adsorbed species, and UV-Vis spectroscopy, which gives details on the metal coordination environment.

In this contribution, to unravel the synthesis mechanism of CeO_2-CuO-based catalysts and to relate their preparation to the catalytic NH_3-SCR performance, we used *in situ* DRIFT, UV-Vis, and Raman spectroscopies, as well as online FTIR monitoring of the gas-phase composition. To allow for a detailed understanding of the aspects controlling the synthesis and reactivity behavior, we will focus on samples with a Ce:Cu mole ratio of 1:1 loaded on silica SBA-15 by solid-state impregnation. Based on the results, the role of the oxide dispersion and distribution for NH_3-SCR reactivity will be discussed.

2. Experimental

2.1 Chemicals

For the preparation of silica SBA-15 the following chemicals were purchased from Sigma-Aldrich Chemie GmbH (Munich, Germany): triblock copolymer Pluronic P123 (molecular weight = 5800, $EO_{20}PO_{70}EO_{20}$), tetraethylorthosilicate (>99%, TEOS), as well as cerium nitrate (>99%, $Ce(NO_3)_3 \cdot 6H_2O$) and cupric nitrate (>99%, $Cu(NO_3)_2 \cdot 3H_2O$), which served as precursors for CeO_2 and CuO, respectively.

2.2 Preparation

Silica SBA-15 was prepared as described previously.[26] The as-made SBA-15 (asSBA-15) was collected using vacuum filtration und then calcined (12 h) in a muffle furnace heated to 550 °C at 1.5 °C /min to remove the template P123, yielding template-free SBA-15 (tfSBA-15). CeO_2 and CuO were loaded onto asSBA-15 or tfSBA-15 by one-pot solid-state impregnation (SSI) by grinding a mixture of 0.173 g of $Ce(NO_3)_3 \cdot 6H_2O$, 0.096 g of $Cu(NO_3)_2 \cdot 3H_2O$, and SBA-15 (0.225 g of asSBA-15 or 0.108 g of tfSBA-15) under ambient conditions for 30 min (molar ratio Ce:Cu = 1:1). The completely mixed powder was calcined in air at 500 °C (5 h) at a heating rate of 1.5 °C/min. The final powder materials will be referred to as tfSBA-CeCuO and asSBA-CeCuO in the following.

As reference samples, CeO_2 and CuO were separately loaded onto SBA-15 by the same procedures as described above, and will be referred to tfSBA-CeO_2, asSBA-CeO_2, tfSBA-CuO and asSBA-CuO, respectively.

In order to perform the *in situ* characterization during the calcination process, reaction cells were used instead of a furnace (see Scheme 1) during sample preparation. The Harrick cell is customized for IR and UV-vis diffuse reflection spectroscopy. For Raman experiments, a Linkam cell was used (see Scheme 1). Catalytic tests were also performed in the Linkam cell. Details will be given below.

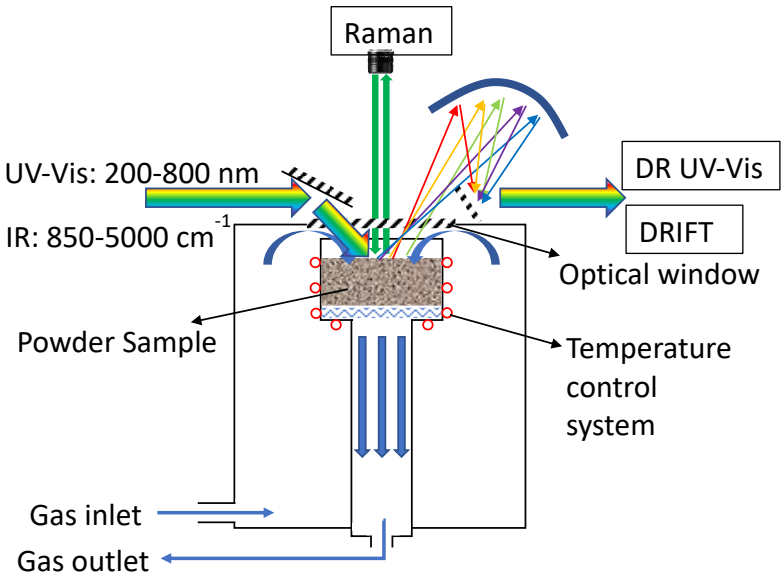

Scheme 1. Schematic diagram of a reaction cell used for *in situ* spectroscopic characterization during catalyst preparation.

2.3 Characterization

For the recordance of X-ray diffraction (XRD) patterns an X-ray powder diffractometer in transmission geometry (StadiP, Stoe & Cie GmbH, Darmstadt, Germany) with a Mythen 1K (Dectris, Baden-Daettwil, Switzerland) detector was employed. Cu Kα1 radiation (λ = 1.540598 Å) and a Ge [110] monochromator were employed, while MPI Jade® software was used for XRD data analysis.

N_2 adsorption/desorption isotherms were measured on a NOVA 3000e system (Quantachrome, Boynton Beach, FL, USA). The calculation of the surface area (S_{BET}) was based on the adsorption data at 0.04-0.2 p/p° and the use of the BET (Brunauer, Emmett, Teller) method. The porosity characteristics were evaluated by using non-local density functional theory (NLDFT).

TEM measurements were performed with a JEOL JEM-2100F (JEOL, Akishimashi, Tokyo, Japan) equipped with a FEG, operating at 200kV. ED spectra and mappings were recorded using an Oxford XMax 80 silicon drift detector (Oxford Instruments plc, Tubney

Woods, Abingdon, U.K.). TEM grids were prepared by dispersing a small amount of sample in 2ml Ethanol with an ultrasonic bath. 3-4 droplets of the suspension were applied on a carbon coated gold grid (Plano GmbH, Wetzlar, Germany) and allowed to dry. The charged grids were lightly carbon coated to avoid charging under the electron beam.

As an X-ray photoelectron spectroscopy (XPS) an SSX 100 ECSA spectrometer (Surface Science Laboratories Inc., Minneapolis, MN, USA) was used, which was equipped with a monochromatic Al-Kα X-ray source (1486.6 eV) and run in constant analyzer energy (CAE) mode at a 36° detection angle (resolution: 0.1 eV). The C 1s peak of ubiquitous carbon (284.9 eV) was used to correct the binding energies. The error in the at.% values (see Table 2) is estimated to be ≤ 0.3. As part of the data analysis a Shirley background was subtracted and a peak-fit analysis was performed using Gaussian−Lorentzian product functions with 45% Lorentzian share. To determine the degree of ceria reduction the ratio $Ce^{3+}/(Ce^{3+}+Ce^{4+})$ was calculated by using the sum of integrated peaks for Ce^{3+} and Ce^{4+}, respectively.

Thermogravimetric analysis (TGA) was performed on a TGA/SDTA851-e (Mettler Toledo). Samples were exposed to a flow of synthetic air (100 ml min^{-1}) during heating from room temperature to 500 °C (rate: 1.5 °C min^{-1}). Then, samples were calcined at 500 °C for 5 h, while at the same time, derivative thermogravimetry (DTG) profiles were obtained.

FTIR spectra were recorded on a Bruker Tensor 27, which was equipped with a DLaTGS (deuterated and L-alanine-doped triglycine sulfate) detector and a low volume gas cell (25 ml, 0.5 m path-length, Axiom). To avoid water condensation during the catalytic reaction the gas cell was heated to 120 °C. IR spectra were continuously recorded every minute (resolution: 4 cm^{-1}). For the analysis backgrounds recorded under pure nitrogen gas were used. The gas-phase concentrations were determined based on a set of calibration curves. For online IR gas-phase detection, we connected the Bruker Tensor to the reactor (commercial CCR1000 catalyst cell, Linkam Scientific Instruments).

For recordance of the diffuse reflectance infrared Fourier transform (DRIFT) spectra a Vertex 70 (Bruker) was used, which was equipped with a liquid N_2 cooled mercury cadmium telluride (MCT) detector and a commercial Harrick cell. As a background standard we used KBr powder. The spectral resolution of DRIFTS was set to 1 cm^{-1}.

Diffuse reflectance (DR) UV-vis spectroscopy was performed on a Jasco V-770 UV-visible/NIR spectrometer, which was equipped with a praying mantis mirror cell, a high-temperature reaction chamber (Harrick Scientific Products Inc.), halogen and deuterium light sources for the visible and ultraviolet, respectively, as well as a Peltier-cooled PbS detector. We recorded spectra from 800 to 200 nm (resolution: 0.5 nm), using MgO as the background standard.

To record visible Raman spectra a Holo Spec f/1.8i spectrometer (Holographic Imaging Spectrograph, Kaiser Optical Systems, USA) was employed, which was equipped with a transmission grating (resolution: of 5 cm^{-1}), while the wavelength stability was better than 0.5 cm^{-1}. For excitation, 532 nm radiation, obtained by frequency doubling from a Nd:YAG laser (Cobolt inc., Germany), was focused onto the sample with a power of 1.6 mW. The Raman scattered light was detected by a Peltier-cooled CCD camera (−40 °C). For *in situ* Raman studies, we used a commercial reactor (CCR1000, Linkam Scientific Instruments, Tadworth, UK) with a quartz glass window.

2.4 Catalytic Performance

To determine the SCR performance of the catalysts (15 mg) we used a commercial CCR1000 reactor (Linkam Scientific Instruments) attached to a FTIR spectrometer for quantitative gas-phase analysis (see above). The inlet gases sources were given as 2000 ppm NO/N_2 (±0.25% abs.), 2000 ppm NH_3/N_2 (±0.25% abs.), O_2 (≥99.999%), and N_2 (≥99.999%), and were adjusted by mass flow controller to be 500 ppm NH_3, 500 ppm NO, and 5 vol.% O_2, and balanced with N_2. The total flow rate was 50 $ml \cdot min^{-1}$, resulting in a gas hourly space velocity (GHSV) of

60000 h^{-1}. For the SCR catalytic test at different temperatures, nine temperatures with 50 °C gradient were set up from 100 to 500 °C. Each temperature step contains for 30 min and the heating rate was set as 30 °C/min.

Using the concentrations of NO, NO_2, N_2O, and NH_3 detected in the outlet gas flow, and the feed gas concentrations, we calculated the N_2 concentration based on conservation of mass and by assuming that nitrogen is present only in the form of the gases listed above. The following equations were used to calculate the NO_x conversion and N_2 selectivity:

$$NO_x \text{ conversion} = \frac{[NO_x]_{in} - [NO_x]_{out}}{[NO_x]_{in}} \times 100\% \quad (1)$$

$$N_2 \text{ selectivity} = \frac{[N_2]_{out}}{[N_2]_{out} + [N_2O]_{out}} \times 100\% \quad (2)$$

where the subscripts in and out indicate the inlet and outlet flows of the reactor, respectively.

3. Result and Discussion

3.1 Characterization

Figure 1 shows the N_2 isotherm adsorption/desorption curves, providing insight into the mesoporous and microporous structure of the SBA-15 supported samples. The curve for tfSBA-15 in Fig. 1a is given as a reference and shows typical H1 type behavior with a hysteresis loop at 0.55-0.75 p/p^0, reflecting uniform hexagonal pores and a narrow pore size distribution centered at around 6.3 nm diameter (see Fig. 1b). After cerium or copper oxides were loaded onto the SBA-15 support, the pore volume declined compared with the unloaded sample, resulting from the blocking of surface pores especially micropores. The shapes of the hysteresis loops changed, indicating the transport of solid oxides into the porous matrix. In detail, for the tfSBA-CeO_2 sample, the desorption branch shows two stages: one at p/p^0 of 0.55-0.7 p/p^0, corresponding to open pores, and another one at 0.4-0.5 p/p^0, suggesting narrow pores due to the local growth of CeO_2. This behavior is consistent with the wide pore size distribution (see

Fig. 1b). The tfSBA-CuO sample shows a similar behavior, but with less pronounced stages, which may be attributed to the lower degree of CuO crystallization and agglomeration compared to CeO_2 (see Fig. S1). For tfSBA-CeCuO, the pore volume further declined as compared to the single cerium or copper oxide loaded samples. In comparison, samples calcined with asSBA-15 (asSBA-CeO_2 and asSBA-CeCuO) showed a better preservation of the pore structure. Similarly, the first stage at 0.6-0.7 p/p^0 is attributed to the open pores, while the second stage, at 0.45-0.6 p/p^0, results from a decreased pore diameter due to the presence of oxides. Overall, the isotherm profiles and porosity characteristics indicate that the asSBA-15-based samples contain more dispersed oxides than the ones based on tfSBA-15. Table 1 summarizes the BET surface area and porosity results of bare SBA-15 and SBA-15 supported cerium and/or copper oxides samples.

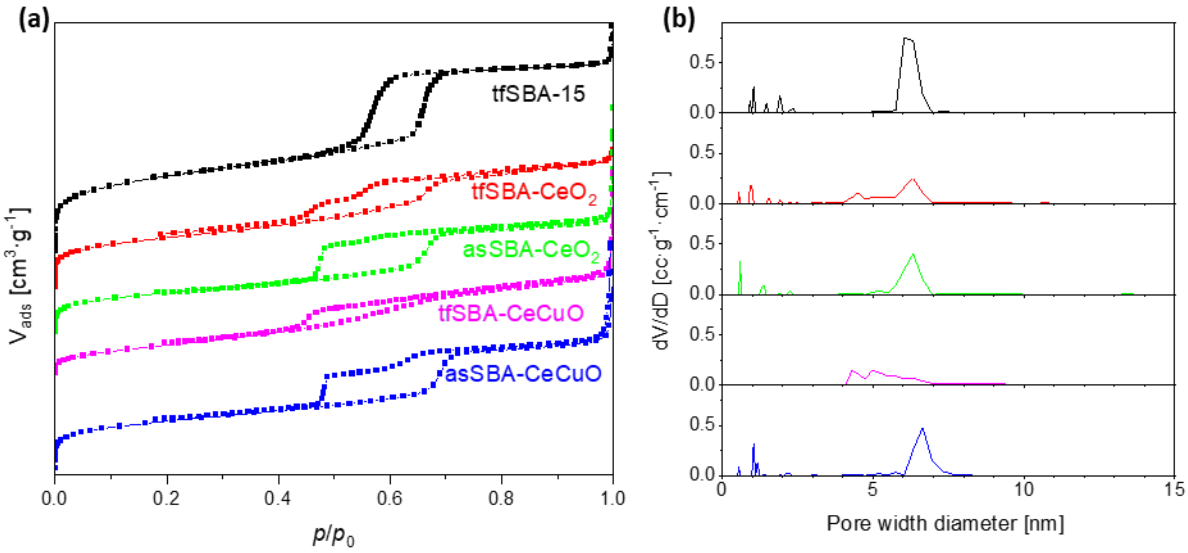

Figure 1. (a) N_2 adsorption/desorption isotherms, and (b) NLDFT pore size distributions of template-free SBA-15- and SBA-15-based materials.

Table 1. Composition, specific surface area, and porosity characteristics of the SBA-15 supported oxide samples compared to bare SBA-15.

Samples	CeO_2 (wt.%)	CuO (wt.%)	S_{total} [m^2/g][a]	D_p [nm][b]	V_{total} [cm^3/g][c]	$đ_{CeO2}$ [nm][d]	$đ_{CuO}$ [nm][d]
tfSBA-15	0	0	616	6.3	0.64	--	--
tfSBA-CeO_2	39	0	414	6.3	0.43	7.2 ± 2.2	--

asSBA-CeO_2	39	0	359	6.3	0.39	7.0 ± 2.1	--
tfSBA-CuO[e]	0	23	445	5.8	0.55	--	20.0 ± 3.9
asSBA-CuO[e]	0	23	315	5.4	0.45	--	--
tfSBA-CeCuO[f]	32	18	285	6.3	0.35	7.0 ± 1.3	--
asSBA-CeCuO[f]	32	18	400	6.6	0.44	5.8 ± 1.0	12.2 ± 7.8

[a] Total BET surface area.

[b] Pore diameter determined from the adsorption branch by NLDFT.

[c] Total pore volume.

[d] Calculated from XRD results using the Scherrer formula. The three strongest peaks were chosen to determine the average crystallite size of CeO_2 and CuO as well as the errors.

[e] N_2 adsorption analysis performed on an Autosorb-3B device.

[f] For sample preparation a different SBA-15 batch was used (S_{total} = 739 m^2/g; D_p = 6.6 nm), explaining the systematically higher surface area and porosity values.

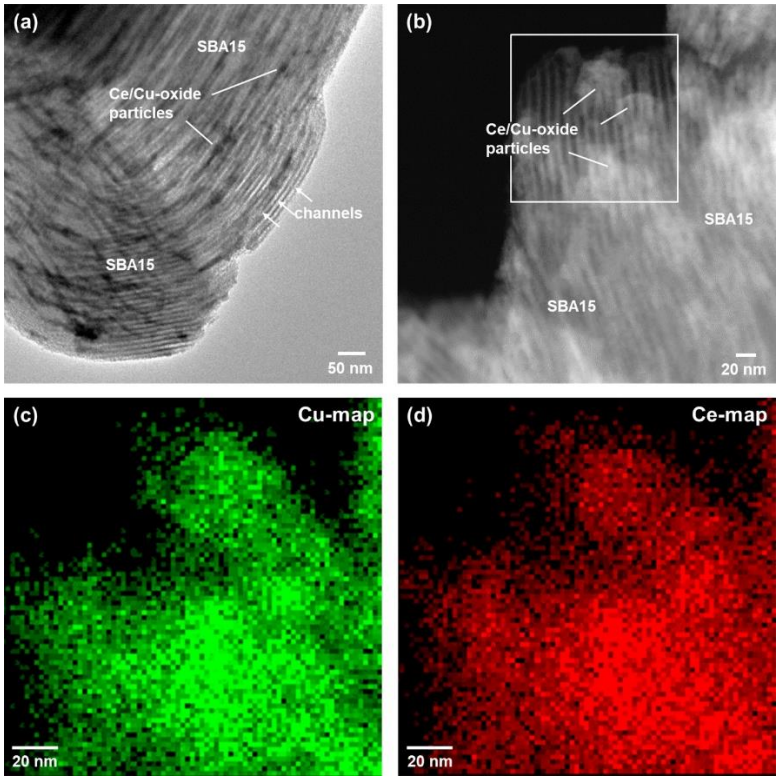

Figure 2. TEM analysis of tfSBA-CeCuO. (a) Bright field, (b) dark field, and elemental mapping of (c) Cu, and (d) Ce, based on the area outlined in (b).

Figure 2 depicts TEM results of the calcined tfSBA-CeCuO sample. The bright field image in Fig. 2a verifies the channel structure of SBA-15. The dark field image in Fig. 2b provides an

enlarged view, indicating that Ce/Cu oxides are mainly located inside the channels but also form particles. Element mapping of Cu and Ce (see Figs. 2c and 2d) reveals that Cu and Ce are well mixed and distributed within SBA-15.

Figure 3 shows the wide-angle XRD patterns of the SBA-15 supported ceria or/and copper oxide samples. The broad diffraction peak at 2θ = 23° observed for template-free SBA-15 is assigned to the amorphous silica framework.[27] After ceria loading, new peaks appear at 28.5°, 33.2°, 47.5°, and 56.3° for both tfSBA-CeO_2 and asSBA-CeO_2, which are readily attributed to crystalline CeO_2.[23] After copper oxide loading, sample tfSBA-CuO shows a series of peaks at 32.67° (110), 35.63° (111), 38.90° (022), 48.83° (202), 53.60° (020), 58.24° (202), 61.59° (113), 66.5° (022), and 68.19° (220), corresponding to different planes of monoclinic CuO.[28] In contrast, sample asSBA-CuO shows no copper oxide–related signals, which indicates that the presence of template P123 makes a difference regarding the copper oxide dispersion, consistent with the different colors observed for tfSBA-CuO (grey) and asSBA-CuO (green). For the co-impregnated sample tfSBA-CeCuO, XRD shows only CeO_2 features with a higher FWHM than those of tfSBA-CeO_2. This implies that Cu^{2+} ions can enter the CeO_2 crystal lattice due to their smaller radius (Cu^{2+}: 72 pm; Ce^{4+}: 92 pm),[29] or form highly dispersed CuO clusters.[30] In contrast, asSBA-CeCuO shows XRD peaks of both CeO_2 and CuO, evidencing the coexistence of crystalline CeO_2 and CuO. Table 1 summarizes the corresponding crystallite sizes, as estimated from the Scherrer equation.

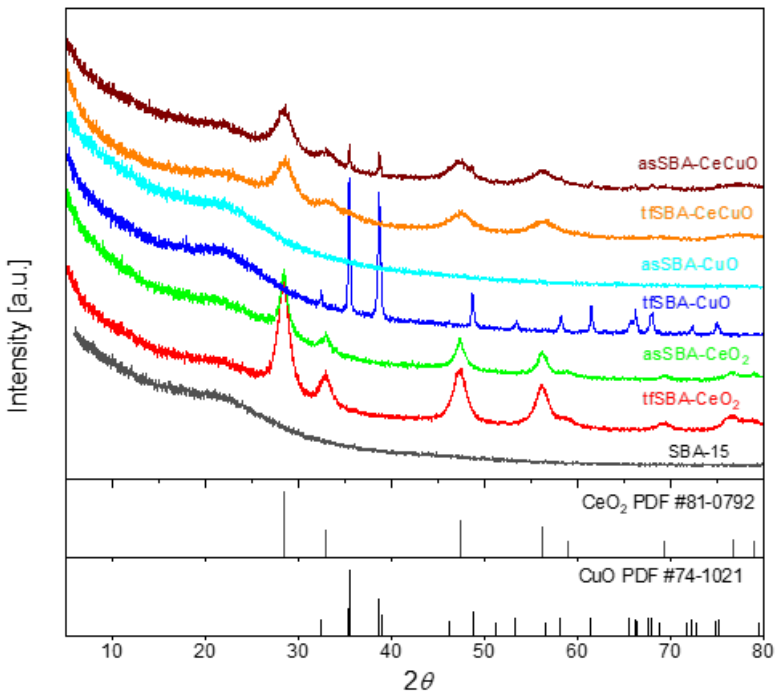

Figure 3. X-ray diffraction patterns of bare SBA-15 and the SBA-15 supported samples.

The XP spectra of the calcined samples provide insight into the surface chemical states of the loaded CeO_2 and CuO. The Ce 3d photoemission presented in Figure 4a is characterized by two sets of peaks from spin–orbit coupling ($d_{3/2}$, $d_{5/2}$), labelled u and v, corresponding to the mixing of Ce^{4+} final states (u, v, u″, v″, u‴, v‴) as well as Ce^{3+} final states (u′, v′, u_0, v_0).[31] On the basis of the Ce 3d XPS data, the surface Ce^{3+} content is determined as 1.4 at.% and 1.5 at.% for tfSBA-CeCuO and asSBA-CeCuO, respectively (see Table 2). Detailed analysis of the Cu 2p photoemission reveals contributions from Cu^{+} and Cu^{2+}, as shown in Figure 4b. The peaks at 953.7 eV and 933.6 eV are assigned to Cu^{2+} $2p_{1/2}$ and Cu^{2+} $2p_{3/2}$ of CuO, respectively.[32] The contributions at lower binding energies can be attributed to the Cu^{+} ion in Cu_2O , while the features at higher binding energies are assigned to Cu^{2+} in $Cu(OH)_2$ formed via thermohydrolysis, in agreement with the literature.[33] The surface compositions of tfSBA-CeCuO and asSBA-CeCuO are summarized in Table 2. The Cu/Ce surface ratio is close to 1 for tfSBA-CeCuO, but equal to 0.6 for asSBA-CeCuO, indicating that tfSBA-CeCuO is characterized by a uniform mixture of metals and asSBA-CeCuO rather than by a phase-

separated structure. In addition, asSBA-CeCuO contains a higher fraction of $Cu(OH)_2$ and Cu_2O, which may originate from hydrolysis and a reducing atmosphere in the presence of P123.

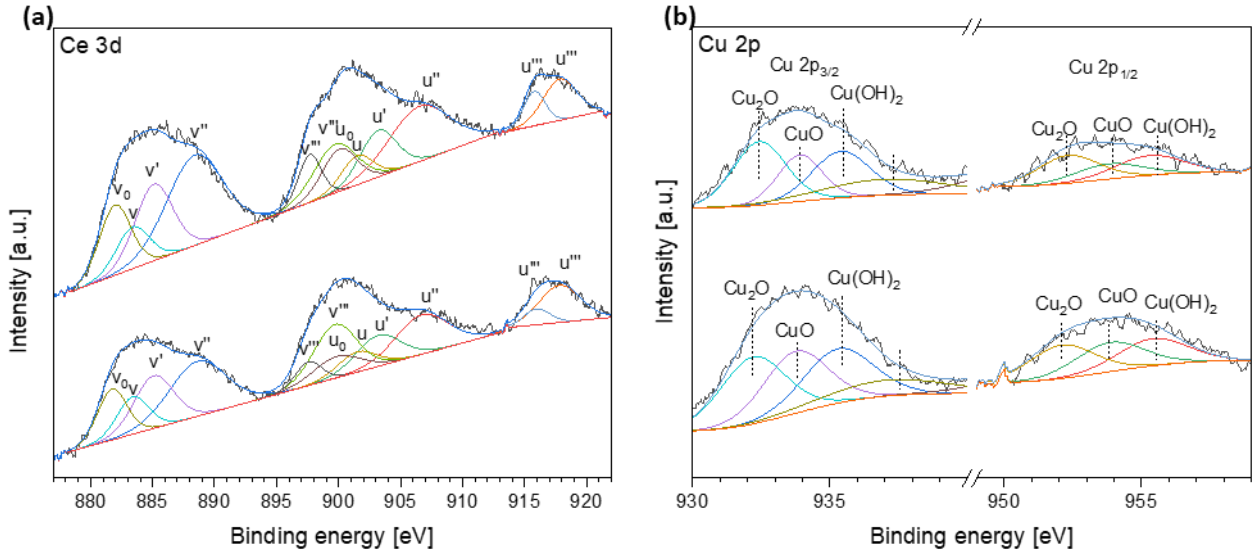

Figure 4. X-ray photoelectron (XP) spectra of tfSBA-CeCuO and asSBA-CeCuO, showing the (a) Ce 3d and (b) Cu 2p photoemission, together with the results of a least-squares fitting analysis. For details see text.

Table 2. Surface composition of tfSBA-CeCuO and asSBA-CeCuO from XPS analysis.

	Elements (at.%)			**Ce^{3+}/ (Ce^{3+} + Ce^{4+})**	**Cu species (at.%)**		
	Cu	**Ce**	**Si**		**$Cu(OH)_2$**	**CuO**	**Cu_2O**
tfSBA-CeCuO	1.5	1.4	23.8	0.33	31.3	32.7	36.0
asSBA-CeCuO	0.9	1.5	25.0	0.34	33.3	25.2	41.5

3.2 Catalytic Tests

Figures 5 and S2 show the catalytic performance of the synthesized samples for NH_3-SCR within the temperature range 100–500 °C. From Fig. 5 it can be clearly seen that e.g. the mono-

metallic oxides tfSBA-CeO_2 and tfSBA-CuO are characterized by a low level of NO_x conversion (maximum: ~30%), while the bimetallic oxides tfSBA-CeCuO and asSBA-CeCuO show a strongly improved NO_x conversion up to ~80 % (see Fig. 5a). Furthermore, tfSBA-CeCuO shows a better low-temperature NO_x conversion at 200-250 °C, while the SCR performance of asSBA-CeCuO spans a wide temperature window ranging from 250 to 450 °C and peaks at around 350 °C. Within the regions of maximum NO_x conversion, both catalysts show N_2 selectivity of 80% or higher (see Fig. 5b). Please note that at 500 °C, the NO_x conversion of the tfSBA-15 prepared samples shows negative values, leading to increased NO_x ($NO+NO_2$) compared with the inlet gas, implying that NH_3 was over-oxidized to NO_2.

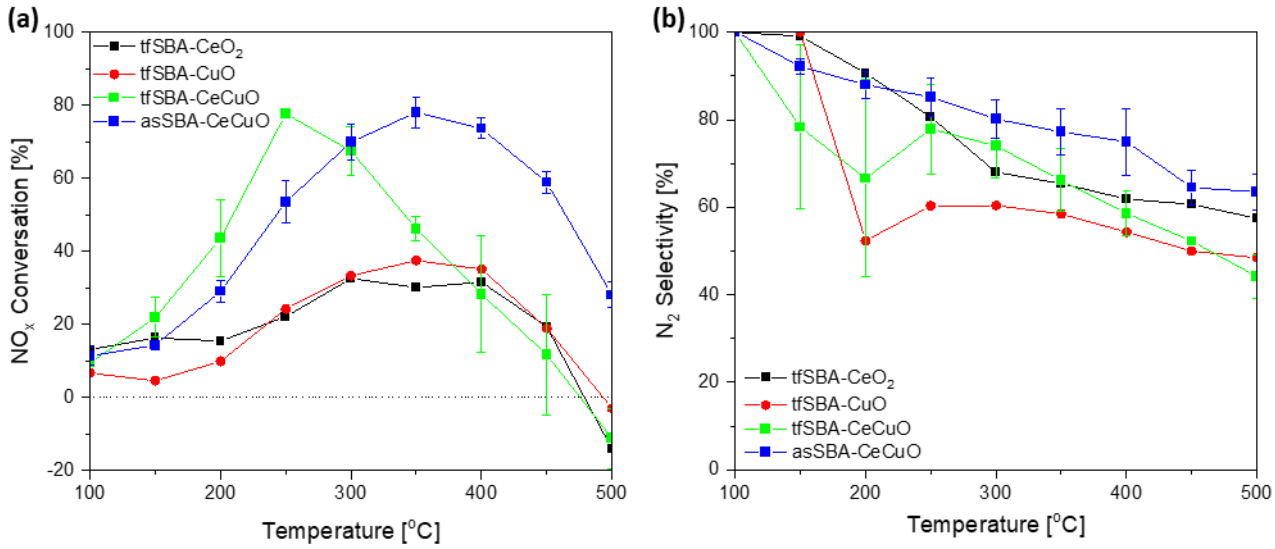

Figure 5. Temperature-dependent NH_3 SCR performance for the synthesized samples: (a) NO_x conversion, (b) N_2 selectivity.

A more detailed view of the NH_3-SCR reactivity behavior of tfSBA-CeCuO and asSBA-CeCuO is provided by Fig. S3, showing the online gas-phase IR during a stepwise increase in temperature. Within the low-temperature range of 150–250 °C, tfSBA-CeCuO clearly shows NO desorption peaks when the temperature is raised, in contrast to asSBA-CeCuO, implying a better low-temperature NO_x conversion by reaction of adsorbed NO with NH_3. Both samples

exhibit similar NH_3 peaks, indicating extensive NH_3 adsorption on the surface, which excludes acidity effects. Regarding the NO_2 emission behavior, major differences between the samples are detected. For tfSBA-CeCuO, NO_2 desorption peaks appear within the whole temperature range studied, while asSBA-CeCuO shows only low-temperature NO_2 peaks. From the observed behavior we deduce that tfSBA-CeCuO is characterized by a stronger oxidizing power, which facilitates the NO_x conversion at low temperatures but increases the transformation of NH_3 into NO_2 at high temperatures, resulting in lower high-temperature NO_x conversion and N_2 selectivity.

3.3 Mechanism of Cerium and Copper Co-dispersion Within the SBA-15 Matrix

As discussed above, the samples tfSBA-CeCuO and asSBA-CeCuO present two types of CuO-CeO_2 materials with improved SCR performance compared to monometallic oxides. While different reactivities of CuO-CeO_2 catalysts have been reported in the literature, a knowledge-based synthesis approach aiming at dedicated surface and catalytic properties is still lacking, hampering further catalyst development. To gain insight into the mechanism of catalyst preparation, we conducted a multiple *in situ* spectroscopy study, as described in the following.

Figure 6 depicts results from the TG analysis of cerium and/or copper nitrate mixed with tfSBA-15 or asSBA-15, using the same experimental conditions as during catalyst preparation. As a reference, the decomposition behavior of bare cerium nitrate, copper nitrate and asSBA-15 is shown in Fig. S4. To identify the critical temperatures, the first derivatives of the TG curves were taken (see Fig. 6b). The critical temperature for template removal of asSBA-15 is about 130 °C. Both cerium nitrate and copper nitrate exhibit two weight losses: The first band at 0–150 °C originates from the loss of water of crystallization, and the second one from decomposition of nitrate salt, which was detected at about 220 °C for $Ce(NO_3)_3$ and 180 °C for $Cu(NO_3)_2$ due to different electronic interactions between metal and nitrate.[34] The higher

charge density of Cu^{2+} effectively polarizes nitrate, facilitating the decomposition compared to Ce^{3+}. In addition, nitrate decomposition is sensitive to other factors, such as the support effect and the calcination atmosphere. For tfSBA-CeO_2 or asSBA-CeO_2, the catalytic interaction between the SiO_2 support or template P123 with cerium nitrate facilitates the nitrate decomposition by changing the metal-nitrate electronic structure, as discussed previously.[34-36] On the other hand, the decomposed P123 creates a reduced atmosphere for asSBA-CeO_2 that can inhibit the nitrate salt decomposition.[37] Thus, the weight loss for the decomposition of $Ce(NO_3)_3$ moves to 200 °C for tfSBA-CeO_2 but is delayed to 250 °C for asSBA-CeO_2. For tfSBA-CuO or asSBA-CuO, dehydration is accompanied by thermohydrolysis, resulting in the appearance of $Cu_2(OH)_3NO_3$, as also discussed later [38] The existence of P123 provides more -OH and free water for the thermohydrolysis products. The final product of the thermolysis, CuO, is formed at 200–250 °C. Finally, for the bimetallic tfSBA-CeCuO or asSBA-CeCuO, the nitrate decomposition temperatures are influenced by the mixed metal cations and the chemical surroundings, including support surface, reduced atmosphere, and moisture.[36, 39] For tfSBA-CeCuO, the weight loss at low temperature (<150 °C) is attributed to water evaporation. After that, $Ce(NO_3)_3$ and $Cu(NO_3)_2$ are gradually decomposed to their oxides at lower decomposition temperatures compared to bare nitrate, owing to the support effect. In the case of asSBA-CeCuO, the increasing temperature makes template P123 lose water and shrink to the silica surface, facilitating the thermohydrolysis of Ce^{3+} and Cu^{2+} as $M(OH)_x(NO_3)_y$, which disperses and fixates the metal ions within the pores. When the temperature reaches about 250 °C, the intermediate $M(OH)_x$ is calcined, thereby forming oxide crystals, as indicated by a sharp decrease in the weight loss curve (see Fig. 6).

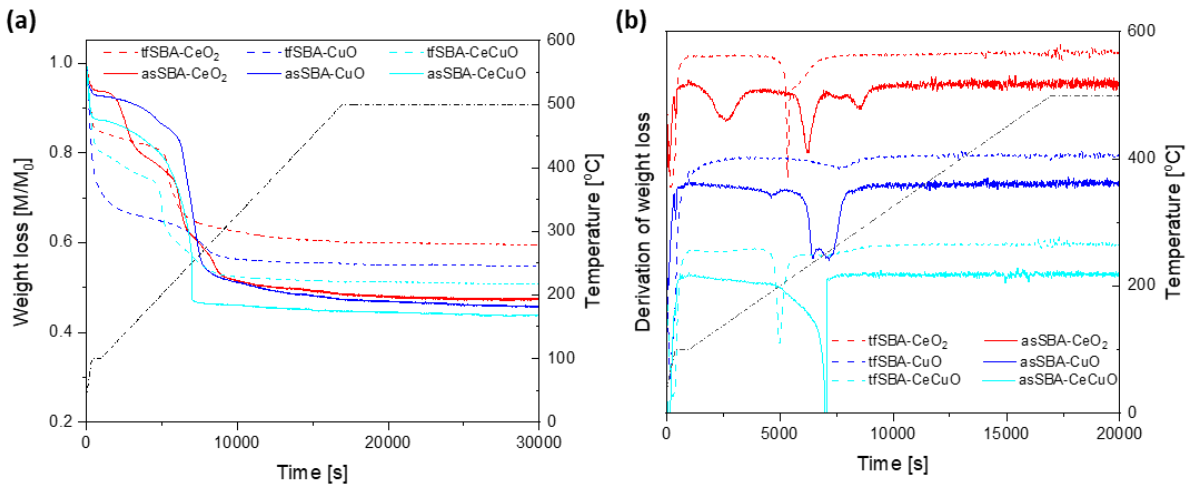

Figure 6. (a) Thermogravimetric analysis (TGA) and (b) Differential thermogravimetric (DTG) of the precursor samples using an airflow of 100 ml/min and the same heating program as during the calcination treatment.

Figure 7 shows online gas-phase IR spectra during air calcination of the precursor samples to tfSBA-CeCuO and asSBA-CeCuO in the temperature range 25–500 °C. In the case of calcination of the precursor of tfSBA-CeCuO (see Fig. 7a), bands at 1316/1340 cm^{-1} and 1698/1716 cm^{-1} are detected at low temperature (~80 ºC), which are assigned to C-O-C bending and C=O stretching vibrations, respectively, accompanied by minor water-related features (1300–1800 cm^{-1}; 3500–4000 cm^{-1}). This implies that the residual template in tfSBA-15 is catalytically decomposed and oxidized by the Ce^{3+} and/or Cu^{2+} nitrate salts. Compared with the results for tfSBA-CeO_2 (see Fig. S5), the presence of copper decreases the critical decomposition temperature of the residual template and changes the reactivity behavior, leading to products containing both C-O-C and C=O groups rather than only C=O groups, as a result of enhanced oxidation. After the catalytic decomposition of residual template, there are two stages of nitrate salt decomposition via $MO_x(NO_3)_y$ (M = Ce and Cu), leading to the release of NO_2 gas at about 170 °C and 200 °C, as observed by the IR signal at 1625 cm^{-1}.[38] Fig. 7a also shows that when the temperature reaches 180 °C and 205 °C, bands due to C-containing products appear at 1316/1340 cm^{-1} (C-O-C), 1698/1716 cm^{-1} (C=O), 2870–2930 cm^{-1} (C-H),

and 2338/2362 cm^{-1} (CO_2), indicating that the produced intermediate $MO_x(NO_3)_y$ and their oxides MO_x can catalyze the decomposition of residual P123 or its segments left inside the pore. For the calcination of the precursor of asSBA-CeCuO (see Fig. 7b), weak signals appear at low temperature (90 °C), which are related to C-O-C (1316/1340 cm^{-1}) and C=O (1689/1716 cm^{-1}) vibrations, followed by NO_2-related signals in the range 100–210 °C. At temperatures >200 °C, H_2O and CO_2 bands are detected together with CH_n stretching features (2790–3950 cm^{-1}) within a narrow temperature range at around 195 °C, in agreement with the TGA results discussed above. Based on the TGA and gas phase IR results, we propose that $Ce(NO_3)_3$ and $Cu(NO_3)_2$ are transferred into the pores to undergo thermohydrolysis and coordinate with -OH groups of P123 as $M(OH)_x(NO_3)_y$ and further hydroxides $M(OH)_x$. Finally, the coordinated metal cations catalytically decompose the P123 template bed with a large number of contact sites while transforming themselves into oxide phases. Summarizing, for tfSBA-CeCuO, a gradual emission is observed, which is attributed to the thermal decomposition of nitrate ligands, while the formation of asSBA-CeCuO is characterized by low temperature NO_2 and high temperature H_2O emission, originating from the hydrolysis of nitrate to hydroxides and condensation of hydroxides to oxides, respectively.

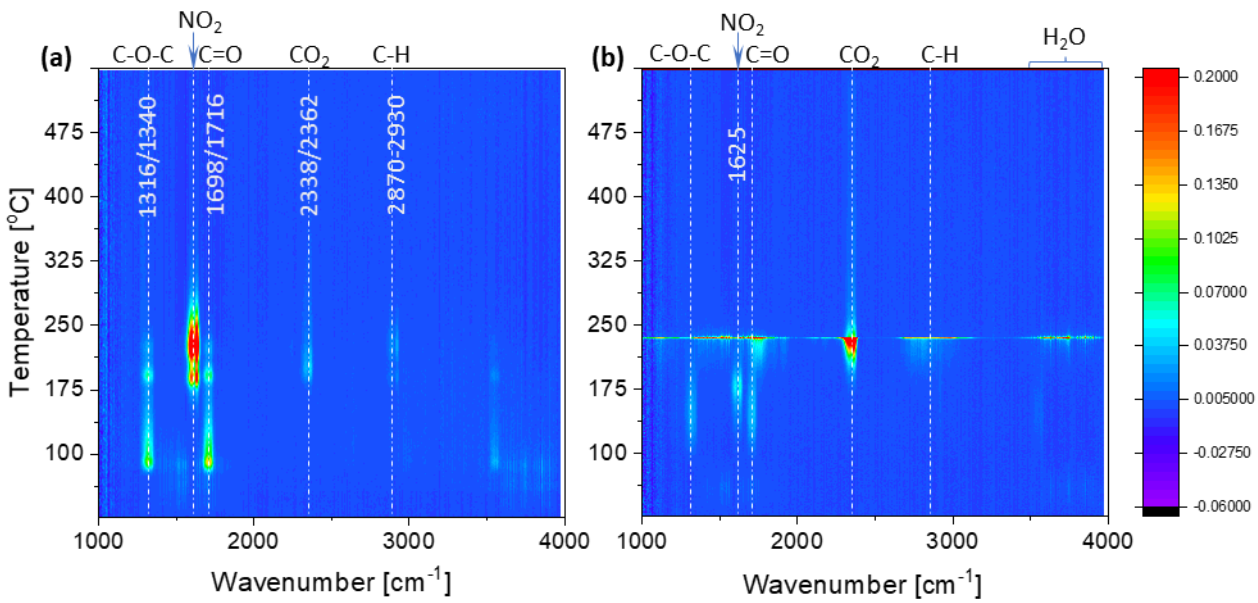

Figure 7. Online IR detection of exhaust gases during air calcination of precursors of the (a) tfSBA-CeCuO, (b) asSBA-CeCuO samples. The temperature was raised from 25 °C to 500 °C at a heating rate of 1.5 °C /min.

To examine the adsorbed species during air calcination, we recorded DRIFT spectra of the precursors to samples tfSBA-CeCuO and asSBA-CeCuO, while the temperature was increased from 25 to 500 °C. For the precursor of tfSBA-CeCuO, at room temperature, strong adsorption bands are observed at 3000–3600 cm^{-1} (see Fig. 8a), which are assigned to H-bonded hydroxyl groups.[40] The presence of water is indicated by the bending and stretching features at around 1640 cm^{-1} and 3442.[40] The sharp but asymmetric peak at 3740 cm^{-1} is characteristic of isolated Si-OH on the surface of silica (SBA-15),[23] whereas the bands at 1036 and 1216 cm^{-1} are attributed to stretching vibrations of the mesoporous framework (Si-O-Si).[41] The DRIFT spectra of the precursor of tfSBA-CeCuO show a series of peaks at 1235, 1342, 1552, 2482/2788, and 2583 cm^{-1}, which are assigned to O-N-O stretching of nitrite,[42] N-O stretching of nitrate,[43] N=O stretching of monodentate nitrate,[42] nitrate species,[44] and nitrite species,[44] respectively. The negative peaks at 2357/2287 cm^{-1} originate from pre-adsorbed CO_2, which gradually desorbs with increasing temperature.[23] The bands at 1759 and 2057 cm^{-1} are attributed to adsorbed nitric oxide and carbon monoxide, respectively,[44, 45] which disappear at temperatures > 235 °C. The nearby bands at 1842 and 1982 cm^{-1} are tentatively assigned to nitrosyl groups coordinated to metal cations.[44] In addition, weak features appear in the NIR region (4000–5000 cm^{-1}, not shown here), originating from the $\nu+\delta$ overtone of M-OH and M-O-M (M = Si, Ce, and Cu) vibrations.[46] When the temperature is increased to 200 °C, the band related to monodentate nitrate at 1522 cm^{-1} decreases, while those related to bidentate nitrate (1554 cm^{-1}) and bridging nitrate (1617 cm^{-1}) increase, indicating a change in coordination from isolated M-O-NO_2 to bridged M-O(NO_2)-M. The band at 1342 cm^{-1} (N-O) shifts to 1296 cm^{-1} (nitrite M-ONO) at 235 °C and finally to 1260 cm^{-1} (chelating nitrate

M-$(O)_2$-NO) at 400 °C, reflecting the decomposition of nitrate salts. As a result of dehydration, starting at 130 °C, the hydroxy-related features in the range 3000–3600 cm^{-1} decrease in intensity. Two weak bands at 3205 and 3489 cm^{-1}, which have been attributed to stretching vibrations of -OH on copper and cerium cations,[46] disappear at temperatures > 235 °C.

The above findings demonstrate that DRIFT spectra provide detailed information on the surface chemistry of tfSBA-CeCuO during calcination. Previously, the thermal decomposition of metal nitrate to metal oxides had been studied by TGA, DTA, conductometric, and thermometric titration methods and proposed to proceed according to the sequence: $M(NO_3)_x \cdot yH_2O \rightarrow M(NO_3)_x \rightarrow MONO_3 \rightarrow CeO_2$.[47] To this end, the IR results of this study provide new insight into the mechanism of metal nitrate decomposition (see Scheme 2), including chelating and bridging rearrangements and final condensation.

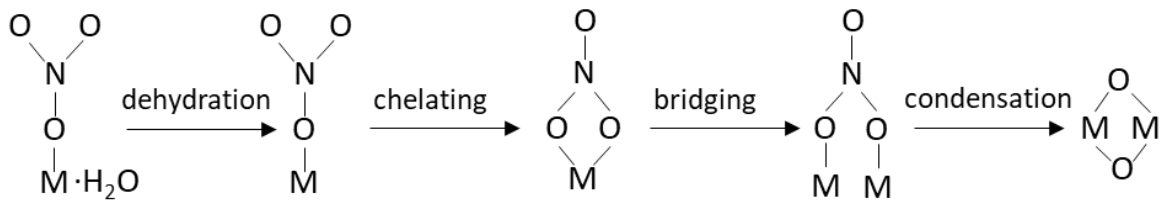

Scheme 2. Schematic process of thermal decomposition of copper and cerium nitrates for tfSBA-CeCuO.

For asSBA-CeCuO (see Fig. 8b), the characteristic C-H stretching features at 2879–2975 cm^{-1} confirm the presence of template P123. The peaks at about 3740 cm^{-1}, which suddenly appear when a critical temperature of 235 °C is reached, are attributed to surface silanol groups.[23] The observed spectral behavior implies that P123 covers the silica surface at low temperature, thereby blocking Si-OH species, while, with increasing temperature, P123 gradually shrinks to the surface and silanol starts to appear (at 235 °C). Correspondingly, the (noisy) features at 800–1500 cm^{-1}, detected at high temperatures, are assigned to C-C bonds resulting from P123 decomposition.[48] The blue-shift of the Ce-OH stretching band from 3373

to 3460 cm^{-1} is assigned to the gradual replacement of nitrate by hydroxyl during the ion-exchange reaction.[40] The spectral region 1500–1600 cm^{-1}, typically assigned to adsorption geometries of nitrate species, reveals that the structure of the nitrate ligands remains unchanged with increasing temperature until 235 °C, where the (intermediate) formation of chelating nitrate (1560 cm^{-1}) is observed. In addition, at temperatures > 235 °C, two new bands appear, at 3232 and 3587 cm^{-1}, which have been attributed to the OH-stretch vibration of copper and cerium hydroxide, respectively.[46] Compared with the apparent spectral changes observed for tfSBA-CeCuO, related to the transformation from monodentate to bridging nitrate and the disappearance of -OH species at high temperature, the presence of P123 (in the case of asSBA-CeCuO) changes the mechanism of nitrate salt decomposition from solid calcination to a hydrothermal-like process,[34] as shown in Scheme 3. To this end, P123 provides abundant -OH and -O- sites to coordinate the metal cations and replace the nitrate by hydroxide ligands by ion exchange.[35] Finally, the metal hydroxides condense to form their oxides.

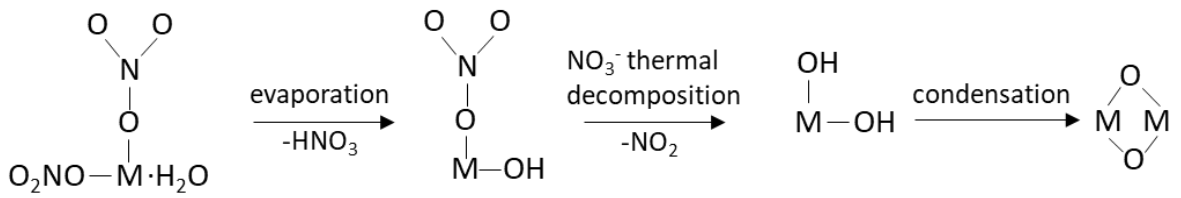

Scheme 3. Schematic process of the hydrothermal-like mechanism for decomposition of copper and cerium nitrate for asSBA-CeCuO.

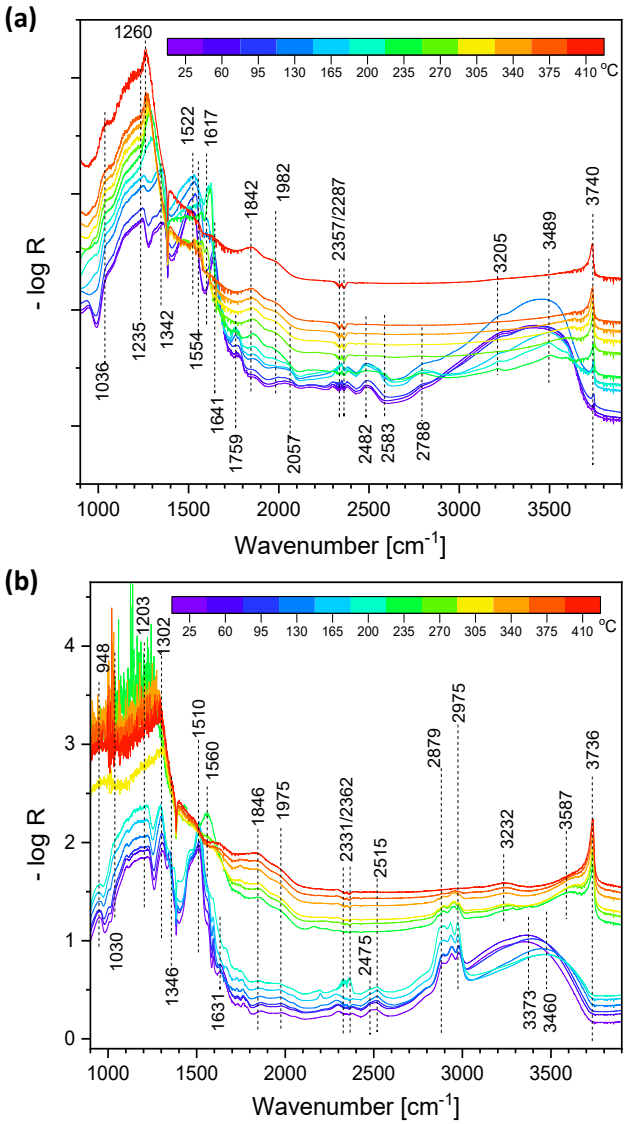

Figure 8. *In situ* DRIFT spectra of precursors of the (a) tfSBA-CeCuO and (b) asSBA-CeCuO samples during air calcination from 25 to 500 °C at a heating rate of 1.5 °C /min.

Figure 9 depicts *in situ* UV-Vis DR spectra of the precursors of tfSBA-CeCuO and asSBA-CeCuO, which allow us to gain insight into changes of the coordination environment of cerium and copper ions during the calcination process. The initial spectra of precursor samples tfSBA-CeCuO and asSBA-CeCuO at low temperature show typical features of $Ce(NO_3)_3$ at 218, 257, and 310 nm, corresponding to a $4f^1$–$5d^1$ electronic transfer of Ce^{3+}, a charge transfer (CT) of O^{2-} 2p to Ce^{3+} 4f/5d, and a CT of Ce^{3+} 5d to O^{2-} 2p, respectively.[49] The broad, weak feature at 600–800 nm is attributed to d-d transitions of Cu^{2+} ions.[50] The ligand metal charge transfer

(LMCT) of O^{2-} 2p to Cu^{2+} 3d shows an absorption band at about 300 nm,[51] which overlaps with the CeO_2 absorption. With increasing temperature, the peak at 257 nm disappears gradually as a result of copper and cerium nitrate decomposition. For tfSBA-CeCuO, the absorption bands at 257 nm and 310 nm increase with increasing temperatures until 225 °C. In the case of asSBA-CeCuO, the peak at 257 nm increases to a stable value at about 250 °C and the bands at about 280–310 nm show an overall increase but an intermediate decrease at 125–175 °C, which is similar to the behavior of the tail bands at 600–800 nm. This behavior suggests that the decomposition of cerium and copper nitrate occurs in different stages, leading to the separate formation of CeO_2 and CuO crystallites. On the other hand, for tfSBA-CeCuO, both nitrates tend to decompose simultaneously and form an amorphous CeO_2-CuO solid solution. A different behavior is also observed for the peaks at about 218 nm, assigned to nitrate ligands, in agreement with the different decomposition routes discussed above. For tfSBA-CeCuO, the features decrease gradually throughout the whole calcination process, corresponding to the successive thermal release of NO_2, while for asSBA-CeCuO, the features show little change until about 250 °C, where a sudden change in the spectral profile is observed due to the formation of oxides, in agreement with the TGA results.

The band gap energy (E_g) was calculated from the DR UV-vis spectra using Eq. 3:[52]

$$\alpha h\nu = A(h\nu - E_g)^n \qquad (3)$$

α is the absorption coefficient, which is determined by the absorbance, and A is a constant. For evaluation of the direct bandgap of the CeO_2-CuO samples, n was taken to be ½.[52] Using Tauc's method, the evolution of the E_g value during calcination can be derived (see Fig. S6). Although the calculation of the bandgap for mixed CuO-CeO_2 is not rigorous, the derived E_g values are still expected to provide a first indication on the doping degree of Cu ions into the CeO_2 lattice by comparison with bare CeO_2 (3.2 eV). The smaller (final) band gap of tfSBA-CeCuO (2.55 eV) compared to asSBA-CeCuO (2.80 eV) thus indicates that the ceria–copper

oxide mixture exhibits a better reducibility, in agreement with the improved catalytic activity at low temperature but minor NO_x conversion at high temperature due to eased oxidation.

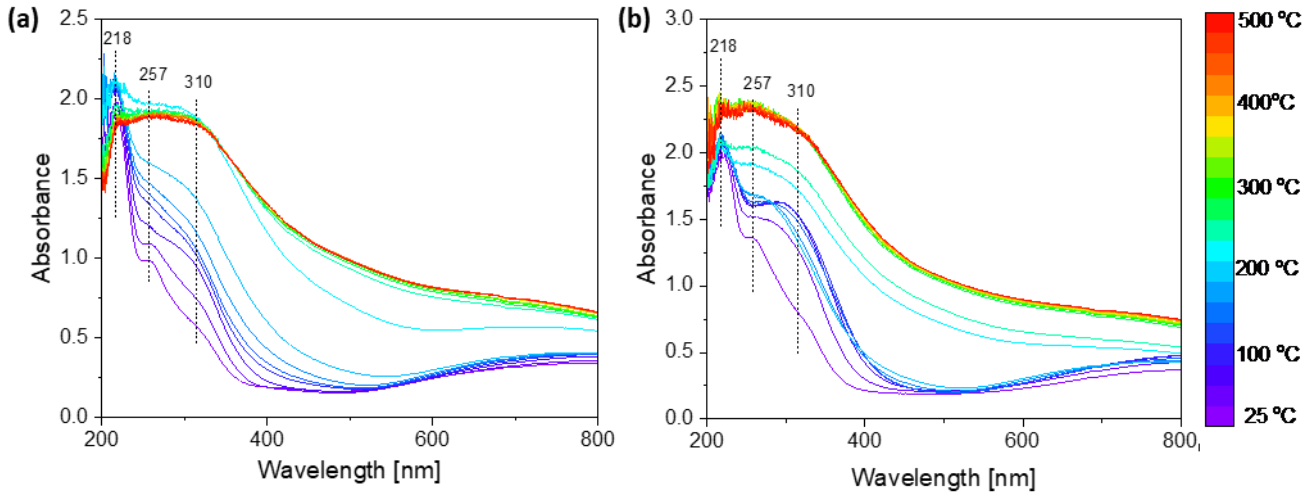

Figure 9. *In situ* UV-Vis DR spectra of precursors of (a) tfSBA-CeCuO, (b) asSBA-CeCuO during air calcination from 25 to 500 °C at a heating rate of 1.5 °C /min.

Figure 10 shows *in situ* Raman spectra of the precursors of tfSBA-CeCuO and asSBA-CeCuO, facilitating the identification of structural changes during the calcination process. Free nitrate is planar and possesses D_{3h} symmetry, resulting in the following vibrational modes: ν_1, symmetric NO stretch at ~1049 cm^{-1}; ν_2, out-of-plane rocking mode at ~830 cm^{-1} (Raman inactive); ν_3, antisymmetric N–O stretch at ~1370 cm^{-1} and ν_4, in-plane deformation at ~719 cm^{-1}. The ν_3 and ν_4 vibrations are doubly degenerate, i.e., they might split upon symmetry lowering.[53] For bulk metal nitrates, nitrates can be coordinated in different ways, e.g. as monodentate, bidentate or tridentate nitrate. For mono- and bidentate nitrates the symmetry is lowered to C_{2v}. As a result, six vibrational modes are expected.[53] Starting with precursor tfSBA-CeCuO, the bands at 720/741 cm^{-1} originate from nitrate in-plane deformation and the strong peak at 1038 cm^{-1} from the symmetric stretch vibration of NO_3^-.[54] The broad feature at 1337 cm^{-1} is attributed to NO_3^- asymmetric stretching,[55] while that at about 1501 cm^{-1} is assigned to the asymmetric N-O stretching of monodentate nitrate.[53] The weak Raman bands

in the range 200–400 cm^{-1} are attributed to M-O (M = Ce and Cu) vibrations, and the peak at 1609 cm^{-1} to bidentate bridging nitrate.[53] For the precursor of asSBA-CeCuO, the peaks at 735 and 1040 cm^{-1} are again assigned to the bending and stretching of nitrate ions, respectively. In contrast, for tfSBA-CeCuO, instead of asymmetric nitrate features (1337, 1501 cm^{-1}), split bands are detected at 1258/1347 and 1455/1513 cm^{-1}. The doublet has been found to be insensitive to the nature of the cation. Thus its structure seems unlikely to be due to ion-pair formation. As the origin of the band splitting, we rather propose the presence of specific NO_3^- ⋯H_2O hydrogen-bond interactions.[56]

In the case of asSBA-CeCuO, additional bands are detected due to the presence of P123. In particular, the features at 814, 854, 930, 956, and 1127 cm^{-1} are attributed to C-O-C symmetric stretching, -CH_3 wagging, C-C symmetric stretching, -CH_3 out of plane bending, and -CH_3 rocking, respectively.[57] The band at 294 cm^{-1} is attributed to Cu-ONO_2 or Ce-ONO_2 vibrations.[58, 59] With increasing temperature, the Raman bands of the precursor of tfSBA-CeCuO continuously decrease in intensity and disappear at about 250 °C, indicating thermal decomposition of $Ce(NO_3)_3$ and $Cu(NO_3)_2$ to their amorphous oxides. In the case of asSBA-CeCuO, the nitrate redshift from 1040 to 1019 cm^{-1} indicates major changes in the vicinity of the nitrate ligands. Previously, Xu et al. discussed metal–nitrate interactions such as hydration and ion pairing effects on the basis of Raman spectra.[54] Jackson et al. reported on the shift of the nitrate symmetric stretch due to partial replacement of nitrate by hydroxyl ligands.[55] Thus, it is reasonable to conclude that the migration of metal cations is supported by P123 and that $M(NO_3)_n$ is coordinated to P123 molecules as $MO(OH)_x(NO_3)_y$.[23, 35] With increasing temperature P123 is then further catalytically transformed to amorphous carbon (band at ~1600 cm^{-1}), which may confine the growth of ceria and copper oxides. The strong change in baseline is due to the formation of amorphous carbon, leading to strong Raman scattering of the sample. After calcination of the precursor of asSBA-CeCuO at 500 °C for 5 h, only one peak is detected at 447 cm^{-1}, which is characteristic of the F_{2g} mode of fluorite CeO_2.

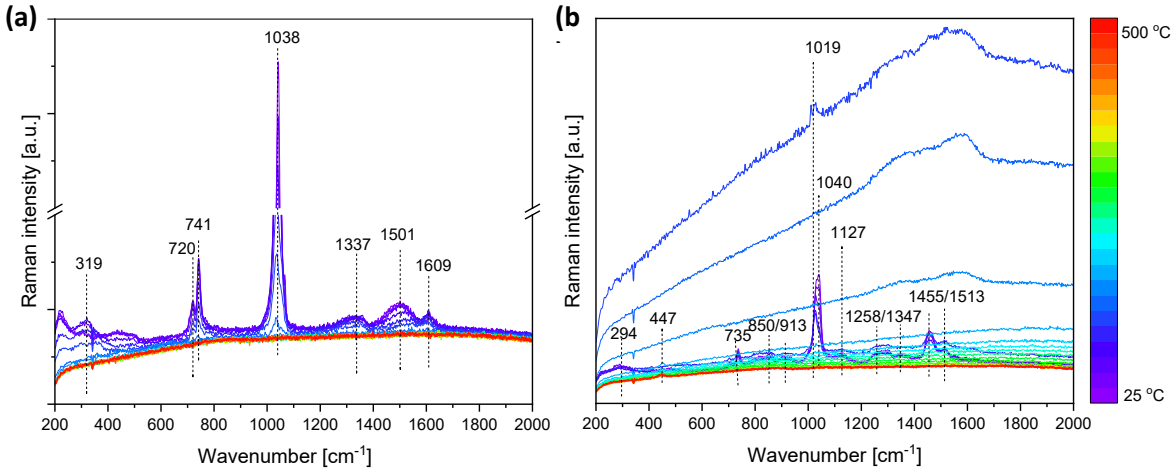

Figure 10. *In situ* Raman spectra of precursors of the (a) tfSBA-CeCuO and (b) asSBA-CeCuO samples during air calcination from 25 to 500 °C at a heating rate of 1.5 °C /min. The spectra were recorded using 532 nm laser excitation.

3.4 Discussion of the Synthesis Mechanism and its Relevance for the Catalytic Properties

In the following, we will first combine the results of the multiple *in situ* analyses during synthesis of CuO-CeO_2 catalysts to develop a comprehensive mechanistic picture, and then discuss their relevance for the catalytic properties. The gas-phase IR results during calcination reveal that tfSBA-CeCuO undergoes a multi-staged release of NO_2 within a wide temperature range (175–320 °C), while asSBA-CeCuO shows NO_2 emission at lower temperature (~175 °C) and a rapid release of H_2O, hydrocarbon, and CO_2 at higher temperature (230 °C) within a narrow temperature window (at about 220–250 °C). This is further supported by TGA showing a multiple step weight loss for tfSBA-CeCuO but a rapid weight loss in one step for asSBA-CeCuO.

The DRIFT spectra provide important information on the transformation and exchange of ligands and the surface chemistry. It is shown that during calcination the precursor of tfSBA-CeCuO decomposes by stepwise NO_2 release, whereas the residual NO_3^- ligands transform from

a monodentate (M-ONO_2) to a bridging (M-O-(N=O)-O-M) structure, which further condenses to mixed metal oxide particles. On the other hand, the decomposition of asSBA-CeCuO follows the hydrothermal-like route, i.e., NO_2 is released during replacement of -ONO_2 by -OH followed by the formation of metal hydroxide $M(OH)_x$, which further condenses as metal oxide.

The *in situ* DR UV-Vis spectra of tfSBA-CeCuO provide evidence for synchronous Ce-O and Cu-O changes, including the formation of bridged Ce-O-(NO)-O-Cu, resulting in an evenly mixed $CeCuO_x$ phase. In contrast, asSBA-CeCuO shows a different behavior supported by the different intermediates during the calcination process, including separated $Ce(OH)_3$ and $Cu(OH)_2$ hydroxyls. *In situ* Raman spectroscopy further specifies the differences of the two routes. The spectra of tfSBA-CeCuO are characterized by features of different nitrate species with monodentate and bridging structures, while for asSBA-CeCuO, a splitting of the asymmetric vibration is observed, implying the presence of hydrolyzed $M(OH)_x(NO_3)_y$ by ligand exchange between NO_3^- and H_2O.

Scheme 4 summarizes the mechanism of CuO-CeO_2 catalyst synthesis as derived from the multiple *in situ* analysis discussed above. In the case of tfSBA-CeCuO (a), cerium and copper nitrates are anchored to the silica surface and nitrates transform into oxides, which involves the conversion of monodentate to bridging nitrate at increasing temperatures and finally the generation of a $CeCuO_x$ solid solution. During the calcination of the asSBA-CeCuO (b) precursor, the nitrate salt is coordinated by OH groups of P123, thereby replacing nitrate ligands. With increasing temperature, P123 shrinks to the silica surface and separates the -OH coordinated metal ions. Finally, $Ce(OH)_3$ and $Cu(OH)_2$ condense separately as CeO_2 and CuO, respectively.

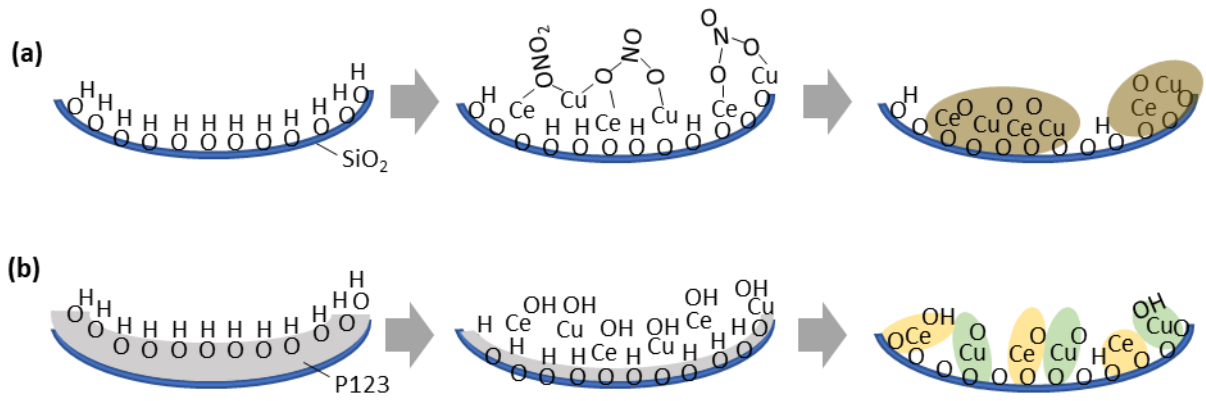

Scheme 4. Mechanism of CuO-CeO_2/SBA-15 catalyst synthesis as deduced from multiple *in situ* analyses without (a) and with (b) the presence of template P123.

In previous studies on CuO-CeO_2 catalysts in the context of CO-PROX, WGS, VOCs, and SCR,[60-63] the superior reactivity of CuO-CeO_2 has been attributed to synergistic effects, originating from strong copper–ceria interactions.[64] To this end, Electronic Metal Support Interactions (EMSI) were proposed to explain the outstanding catalytic performance rather than Strong Metal Support Interactions (SMSI).[65, 66] In the EMSI concept, the alteration of the chemical properties of metal sites is related to perturbations in their electronic properties resulting from bonding interactions with the ceria support. Consequently, the fine-tuning of the copper and ceria oxide morphological characteristics can notably affect the metal–support interactions and, as a consequence, alter the catalytic performance.[64] When copper ions enter the ceria lattice or form smaller clusters on the ceria surface, the interaction between CuO and CeO_2 improves the surface reducibility, while the formation of larger copper oxide aggregates is expected to attenuate the interaction with ceria. Previously,[67] CuO-CeO_2 prepared by Cu doping was investigated for NH_3-SCR of NO, showing an enhanced low-temperature activity, but decreased high-temperature activity owing to NH_3 oxidation. On the other hand, for CuO/$Ce_{0.8}Zr_{0.2}O_2$ catalysts used for NO reduction by CO, the maximum catalytic activity was found to be related to moderate sizes of bulk CuO.[68] Thus, consistent with the literature, the sample tfSBA-CeCuO, which is characterized by a $CeCuO_x$ solid solution, shows considerable

improvement of the low-temperature NO_x conversion, but lower N_2 selectivity due to its strong oxidation. The asSBA-CeCuO contains separated CuO and CeO_2 particles, exhibiting a moderate EMSI effect, which results in an improved SCR catalytic performance at high temperatures and over a wide temperature range.

4. Conclusion

Bimetallic oxides CeO_2-CuO supported on mesoporous SBA-15 for NH_3-SCR applications were prepared by solid-state impregnation and structure–activity relations were established. It is demonstrated that templates can be employed in a targeted manner to influence the structure of the oxides, resulting in different NH_3-SCR properties. The catalyst from the template-free synthesis (tfSBA-CeCuO) is characterized by a CeO_2-CuO solid solution showing better low-temperature NO_x conversion but increased high-temperature NH_3 oxidation, owing to its enhanced oxidation properties by coupled Ce^{3+}/Ce^{4+} and Cu^{+}/Cu^{2+} pairs. The catalyst formed in the presence of the template (asSBA-CeCuO) exhibits smaller but separated oxides phases of CeO_2 and CuO, showing an improved SCR performance within a wide temperature range due to the moderate EMSI effect.

A series of *in situ* analyses was performed to directly monitor the precursor decomposition during calcination, including gas-phase, surface, and bulk changes. In addition to conventional TG analysis, the *in situ* DRIFT spectra provide important information on the transformation and exchange of ligands and the surface chemistry, especially the identification of the nitrate and hydroxide intermediates during the change from metal precursors their oxides. The *in situ* DR UV-Vis spectra give evidence for synchronous or asynchronous Ce-O and Cu-O changes, corresponding to the formation of mixed or separated phases. Additionally, based on detailed analysis of the nitrate vibrations, *in situ* Raman spectroscopy further specifies the different decomposition pathways caused by the presence of different chemical environments. As an

important result, *in situ* spectroscopy evidenced two decomposition routes of the metal nitrates to their oxides, which are characterized by different catalytic properties: the precursor of tfSBA-CeCuO followed a nitrate-bridging mechanism via a Ce-O-(N=O)-O-Cu intermediate and ended as CeO_2-CuO solid solution, while the precursor of asSBA-CeCuO followed a hydrolysis-based mechanism, forming hydroxides $M(OH)_x$ on the route towards separated CeO_2 and CuO.

Generally, the results presented here can be used as a guideline for the development of mesoporous composite oxides by solid-state impregnation methods. The change of synthesis conditions using template assistance enables the dedicated formation of different oxide structures with different catalytic properties. Importantly, *in situ* spectra allowed to directly characterize the structural properties of the formed oxide catalysts and to correlate their structure with the catalytic performance in NH_3 SCR. Based on our study, we expect the use of *in situ* spectroscopy to largely facilitate the rational synthesis of highly active and selective catalyst materials for NO_x abatement as well as other applications.

Acknowledgements

The authors thank Till Wissel and Ott Alexander for N_2 adsorption–desorption measurements, Kathrin Hofmann for XRD analysis, and Karl Kopp for XPS analysis and technical support.

Supporting Information

Additional experimental data on sample characterization and reactivity behavior; N_2-adsorption/desorption isotherms; SCR catalytic test results; online IR gas phase monitoring of SCR reaction; TGA and DTG profiles; analysis of UV-Vis spectra.

References

1. Han, L. P.; Cai, S. X.; Gao, M.; Hasegawa, J.; Wang, P. L.; Zhang, J. P.; Shi, L. Y.; Zhang, D. S. Selective Catalytic Reduction of NO_x with NH_3 by Using Novel Catalysts: State of the Art and Future Prospects. *Chem. Rev.* **2019,** *119*, 10916-10976.

2. Zhan, S. H.; Zhang, H.; Zhang, Y.; Shi, Q.; Li, Y.; Li, X. J. Efficient NH_3-SCR Removal of NO_x with Highly Ordered Mesoporous $WO_3(\chi)$-CeO_2 at Low Temperatures. *Appl. Catal. B-Environ.* **2017,** *203*, 199-209.

3. Zhang, N. Q.; Li, L. C.; Guo, Y. Z.; He, J. D.; Wu, R.; Song, L. Y.; Zhang, G. Z.; Zhao, J. S.; Wang, D. S.; He, H. A MnO_2-based Catalyst with H_2O Resistance for NH_3-SCR: Study of Catalytic Activity and Reactants-H_2O Competitive Adsorption. *Appl. Catal. B-Environ.* **2020,** *270, 118860*.

4. Xu, H. D.; Liu, J. X.; Zhang, Z. H.; Liu, S.; Lin, Q. J.; Wang, Y.; Dai, S.; Chen, Y. Q. Design and Synthesis of Highly-Dispersed WO_3 Catalyst with Highly Effective NH_3-SCR Activity for NO_x Abatement. *ACS Catal.* **2019,** *9*, 11557-11562.

5. Liu, C.; Shi, J. W.; Gao, C.; Niu, C. M. Manganese Oxide-based Catalysts for Low-temperature Selective Catalytic Reduction of NO_x with NH_3: A Review. *Appl. Catal. A-Gen.* **2016,** *522*, 54-69.

6. Cheng, L. S.; Yang, R. T.; Chen, N. Iron Oxide and Chromia Supported on Titania-pillared Clay for Selective Catalytic Reduction of Nitric Oxide with Ammonia. *J. Catal.* **1996,** *164*, 70-81.

7. Chang, H.; Ma, L.; Yang, S.; Li, J.; Chen, L.; Wang, W.; Hao, J. Comparison of Preparation Methods for Ceria Catalyst and the Effect of Surface and Bulk Sulfates on its Activity toward NH_3-SCR. *J. Hazard. Mater.* **2013,** *262*, 782-8.

8. Fan, J.; Jiang, X.; Min, H.; Li, D.; Ran, X.; Zou, L.; Sun, Y.; Li, W.; Yang, J.; Teng, W.; Li, G.; Zhao, D. Facile Preparation of Cu–Mn/CeO_2/SBA-15 Catalysts Using Ceria as an Auxiliary for Advanced Oxidation Processes. *J. Mater. Chem. A* **2014,** *2*, 10654.

9. Bin, F.; Song, C.; Lv, G.; Song, J.; Cao, X.; Pang, H.; Wang, K. Structural Characterization and Selective Catalytic Reduction of Nitrogen Oxides with Ammonia: A Comparison between Co/ZSM-5 and Co/SBA-15. *J. Phys. Chem. C* **2012,** *116*, 26262-26274.

10. Van, N. T. T.; Loc, L. C.; Anh, N. P.; Cuong, H. T.; Tri, N. Positive Effects of CeO_2 Promoter and Co-Reactant/CO on Methanation of CO_2-Rich Gas over Ni/SBA-15 Catalyst. *Mater. Trans.* **2020,** *61*, 1332-1338.

11. Li, G.; Wang, B.; Wang, H.; Ma, J.; Xu, W. Q.; Li, Y.; Han, Y.; Sun, Q. Fe and/or Mn Oxides Supported on Fly Ash-derived SBA-15 for Low-temperature NH_3-SCR. *Catal. Commun.* **2018,** *108*, 82-87.

12. Li, J. S.; Gu, J.; Xia, M. Y.; Yuan, J. F.; Sun, X. Y.; Wang, L. J. Synthesis of SBA-15 Loaded CeO_2 Nanocrystals via Sol-gel One-step Process. *Acta Chim. Sin.* **2008,** *66*, 2305-2308.

13. Oliveira, L. H.; de Barros, A.; Pinto, L. O.; Oliveira, C. S.; Kubota, L. T.; Sigoli, F. A.; Mazali, I. O. Sensitive Colorimetric Assay Based on Peroxidase-Like Activity of CeO_2 Nanoparticles Supported on SBA-15 Mesoporous Silica to Determination of H_2O_2. *Chemistryselect* **2019,** *4*, 2160-2167.

14. Moogi, S.; Lee, I. G.; Hwang, K. R. Catalytic Steam Reforming of Glycerol over Ni-La_2O_3-CeO_2/SBA-15 Catalyst for Stable Hydrogen-rich Gas Production. *Int. J. Hydrogen Energy* **2020,** *45*, 28462-28475.

15. Tang, C. J.; Sun, J. F.; Yao, X. J.; Cao, Y.; Liu, L. C.; Ge, C. Y.; Gao, F.; Dong, L. Efficient Fabrication of Active CuO-CeO_2/SBA-15 Catalysts for Preferential Oxidation of CO by Solid State Impregnation. *Appl. Catal. B-Environ.* **2014,** *146*, 201-212.

16. Zhang, Q. L.; Zhang, T. F.; Shi, Y. Z.; Zhao, B.; Wang, M. Z.; Liu, Q. X.; Wang, J.; Long, K. X.; Duan, Y. K.; Ning, P. A Sintering and Carbon-resistant Ni-SBA-15 Catalyst Prepared by Solid-state Grinding Method for Dry Reforming of Methane. *J. CO_2 Util.* **2017,** *17*, 10-19.

17. Yin, Y.; Wen, Z. H.; Liu, X. Q.; Yuan, A. H.; Shi, L. Functionalization of SBA-15 with CeO_2 Nanoparticles for Adsorptive Desulfurization: Matters of template P123. *Adsorpt. Sci. Technol.* **2018,** *36*, 953-966.

18. Yin, Y.; Tan, P.; Liu, X. Q.; Zhu, J.; Sun, L. B. Constructing a Confined Space in Silica Nanopores: an Ideal Platform for the Formation and Dispersion of Cuprous Sites. *J. Mater. Chem. A* **2014,** *2*, 3399-3406.

19. Taratayko, A.; Larichev, Y.; Zaikovskii, V.; Mikheeva, N.; Mamontov, G. Ag-CeO_2/SBA-15 Composite Prepared from Pluronic P123@SBA-15 Hybrid as Catalyst for Room-temperature Reduction of 4-nitrophenol. *Catal. Today* **2021,** *375*, 576-584.

20. Ning, X.; Lu, Y. Y.; Fu, H. Y.; Wan, H. Q.; Xu, Z. Y.; Zheng, S. R. Template-Mediated Ni(II) Dispersion in Mesoporous SiO_2 for Preparation of Highly Dispersed Ni Catalysts: Influence of Template Type. *ACS Appl. Mater. Interfaces* **2017,** *9*, 19335-19344.

21. Sun, X.; Guo, R. T.; Liu, S. W.; Liu, J.; Pan, W. G.; Shi, X.; Qin, H.; Wang, Z. Y.; Qiu, Z. Z.; Liu, X. Y. The Promoted Performance of CeO_2 Catalyst for NH_3-SCR Reaction by NH_3 Treatment. *Appl. Surf. Sci.* **2018,** *462*, 187-193.

22. Wang, T.; Li, C. T.; Zhao, L. K.; Zhang, J. Y.; Li, S. H.; Zeng, G. M. The Catalytic Performance and Characterization of ZrO_2 Support Modification on $CuO-CeO_2/TiO_2$ Catalyst for the Simultaneous Removal of Hg^0 and NO. *Appl. Surf. Sci.* **2017,** *400*, 227-237.

23. Shen, J.; Hess, C. Controlling the Dispersion of Ceria Using Nanoconfinement: Application to CeO_2/SBA-15 Catalysts for NH_3-SCR. *Mater. Adv.* **2021,** *2,* 7400-7412.

24. Mantella, V; Strach, M.; Frank, K.; Pankhurst, J. R.; Stoian, D.; Gadiyar, C.; Nickel, B.; Buonsanti, R. Polymer Lamellae as Reaction Intermediates in the Formation of Copper Nanospheres as Evidenced by In Situ X-ray Studies. *Angew. Chem. Int. Ed*. **2020**, *132*, 11724-11730.

25. Weber, S.; Diaz, A.; Holler, M.; Schropp, A.; Lyubomirskiy, M.; Abel, K. L.; Kahnt, M.; Jeromin, A.; Kulkarni, S.; Keller, T. F.; Gläser, R.; Sheppard, T. L. Evolution of Hierarchically Porous Nickel Alumina Catalysts Studied by X-Ray Ptychography. *Adv. Sci.* **2022**, *9*, 2105432.

26. Zhao, D. Y.; Sun, J. Y.; Li, Q. Z.; Stucky, G. D. Morphological Control of Highly Ordered Mesoporous Silica SBA-15. *Chem. Mater.* **2000,** *12*, 275-279.

27. Shen, J.; Hess, C. High Surface Area VO_x/TiO_2/SBA-15 Model Catalysts for Ammonia SCR Prepared by Atomic Layer Deposition. *Catalysts* **2020,** *10,* 1386.

28. Frenkel, A. I.; Wang, Q.; Marinkovic, N.; Chen, J. G.; Barrio, L.; Si, R.; Camara, A. L.; Estrella, A. M.; Rodriguez, J. A.; Hanson, J. C. Combining X-ray Absorption and X-ray Diffraction Techniques for in Situ Studies of Chemical Transformations in Heterogeneous Catalysis: Advantages and Limitations. *J. Phys. Chem. C* **2011,** *115*, 17884-17890.

29. Zeng, S. H.; Zhang, W. L.; Sliwa, M.; Su, H. Q. Comparative Study of CeO_2/CuO and CuO/CeO_2 Catalysts on Catalytic Performance for Preferential CO oxidation. *Int. J. Hydrogen Energy* **2013,** *38*, 3597-3605.

30. Yang, Z. X.; Xie, L. G.; Ma, D. W.; Wang, G. T. Origin of the High Activity of the Ceria-Supported Copper Catalyst for H_2O Dissociation. *J. Phys. Chem. C* **2011,** *115*, 6730-6740.

31. Nottbohm, C. T.; Hess, C. Investigation of Ceria by Combined Raman, UV-vis and X-ray Photoelectron Spectroscopy. *Catal. Commun.* **2012,** *22*, 39-42.

32. Gao, D. Q.; Zhang, J.; Zhu, J. Y.; Qi, J.; Zhang, Z. H.; Sui, W. B.; Shi, H. G.; Xue, D. S. Vacancy-Mediated Magnetism in Pure Copper Oxide Nanoparticles. *Nanoscale Res. Lett.* **2010,** *5*, 769-772.

33. Zhu, C. Q.; Osherov, A.; Panzer, M. J. Surface Chemistry of Electrodeposited Cu_2O Films Studied by XPS. *Electrochim Acta* **2013,** *111*, 771-778.

34. Cochran, E. A.; Woods, K. N.; Johnson, D. W.; Page, C. J.; Boettcher, S. W. Unique Chemistries of Metal-nitrate Precursors to Form Metal-oxide Thin Films from Solution: Materials for Electronic and Energy Applications. *J. Mater. Chem. A* **2019,** *7*, 24124-24149.

35. Yang, W. W.; Liu, H. M.; Li, Y. M.; He, D. H. Interaction Mechanism of $Ni(NO_3)_2{\cdot}6H_2O$ and P123 in Preparing Highly-dispersed Ni/SBA-15 Catalytic Materials. *Microporous Mesoporous Mater.* **2016,** *228*, 174-181.

36. Malecka, B.; Lacz, A.; Drozdz, E.; Malecki, A. Thermal Decomposition of d-metal Nitrates Supported on Alumina. *J. Therm. Anal. Calorim.* **2015,** *119*, 1053-1061.

37. Sietsma, J. R. A.; Meeldijk, J. D.; den Breejen, J. P.; Versluijs-Helder, M.; van Dillen, A. J.; de Jongh, P. E.; de Jong, K. P. The Preparation of Supported NiO and Co_3O_4 Nanoparticles by the Nitric Oxide Controlled Thermal Decomposition of Nitrates. *Angew. Chem. Int. Ed.* **2007,** *46*, 4547-4549.

38. Morozov, I. V.; Znamenkov, K. O.; Korenev, Y. M.; Shlyakhtin, O. A. Thermal Decomposition of $Cu(NO_3)_2 \cdot 3H_2O$ at Reduced Pressures. *Thermochim. Acta* **2003,** *403*, 173-179.

39. Yuvaraj, S.; Fan-Yuan, L.; Tsong-Huei, C.; Chuin-Tih, Y. Thermal Decomposition of Metal Nitrates in Air and Hydrogen Environments. *J. Phys. Chem. B* **2003,** *107*, 1044-1047.

40. Seo, J.; Lee, J. W.; Moon, J.; Sigmund, W.; Paik, U. Role of the Surface Chemistry of Ceria Surfaces on Silicate Adsorption. *ACS Appl. Mater. Interfaces* **2014,** *6*, 7388-7394.

41. Sakthivel, A.; Pedro, F. M.; Chiang, A. S. T.; Kuhn, F. E. Grafting of Cyclopentadienyl Ruthenium Complexes on Aminosilane Linker Modified Mesoporous SBA-15 Silicates. *Dalton Trans.* **2007**, *3,* 320-326.

42. Tamm, S.; Vallim, N.; Skoglundh, M.; Olsson, L. The Influence of Hydrogen on the Stability of Nitrates during H_2-assisted SCR over Ag/Al_2O_3 catalysts - A DRIFT study. *J. Catal.* **2013,** *307*, 153-161.

43. Wattanathana, W.; Suetrong, N.; Kongsamai, P.; Chansaenpak, K.; Chuanopparat, N.; Hanlumyuang, Y.; Kanjanaboos, P.; Wannapaiboon, S. Crystallographic and Spectroscopic Investigations on Oxidative Coordination in the Heteroleptic Mononuclear Complex of Cerium and Benzoxazine Dimer. *Molecules* **2021,** *26*, 5410.

44. Hadjiivanov, K. I. Identification of Neutral and Charged N_xO_y Surface Species by IR Spectroscopy. *Catal. Rev. Sci. Eng.* **2000,** *42*, 71-144.

45. Kladis, C.; Bhargava, S. K.; Foger, K.; Akolekar, D. B. Investigations of Nitric Oxide and Carbon Monoxide Adsorption on the New Generation Cerium Exchanged Silico-aluminophosphate of Type 18 Catalyst. *J. Mol. Catal. A-Chem.* **2001,** *175*, 241-248.

46. Hadjiivanov, K. Identification and Characterization of Surface Hydroxyl Groups by Infrared Spectroscopy. *Adv. Catal.* **2014,** *57*, 99-318.

47. Wendlandt, W. W.; Bear, J. L. Thermal Decomposition of the Heavier Rare-Earth Metal Nitrate Hydrates - Thermobalance and Differential Thermal Analysis Studies. *J. Inorg. Nucl. Chem.* **1960,** *12*, 276-280.

48. Sabzehmeidani, M. M.; Karimi, H.; Ghaedi, M. Enhanced Visible Light-active $CeO_2/CuO/Ag_2CrO_4$ Ternary Heterostructures Based on CeO_2/CuO Nanofiber Heterojunctions for the Simultaneous Degradation of a Binary Mixture of Dyes. *New J. Chem.* **2020,** *44*, 5033-5048.

49. Nicolini, V.; Varini, E.; Malavasi, G.; Menabue, L.; Menziani, M. C.; Lusvardi, G.; Pedone, A.; Benedetti, F.; Luches, P. The Effect of Composition on Structural, Thermal, Redox and Bioactive Properties of Ce-containing Glasses. *Mater. Des.* **2016,** *97*, 73-85.

50. Pande, S.; Weir, M. G.; Zaccheo, B. A.; Crooks, R. M. Synthesis, Characterization, and Electrocatalysis Using Pt and Pd Dendrimer-encapsulated Nanoparticles Prepared by Galvanic Exchange. *New J. Chem.* **2011,** *35*, 2054-2060.

51. Pascher, T. F.; Oncak, M.; van der Linde, C.; Beyer, M. K. Spectroscopy and Photochemistry of Copper Nitrate Clusters. *Phys. Chem. Chem. Phys.* **2021,** *23*, 9911-9920.

52. Bosigo, R.; Lepodise, L. M.; Kuvarega, A.; Muiva, C. Hydrothermal Synthesis of CuO and CeO_2/CuO Nanostructures: Spectroscopic and Temperature Dependent Electrical Properties. *J. Mater. Sci.-Mater. Electron.* **2021,** *32*, 7136-7152.

53. Mihaylov, M. Y.; Zdravkova, V. R.; Ivanova, E. Z.; Aleksandrov, H. A.; St Petkov, P.; Vayssilov, G. N.; Hadjiivanov, K. I. Infrared Spectra of Surface Nitrates: Revision of the Current Opinions Based on the Case Study of Ceria. *J. Catal.* **2021,** *394*, 245-258.

54. Xu, M.; Larentzos, J. P.; Roshdy, M.; Criscenti, L. J.; Allen, H. C. Aqueous Divalent Metal-nitrate Interactions: Hydration versus Ion Pairing. *Phys. Chem. Chem. Phys.* **2008,** *10*, 4793-4801.

55. Jackson, M. N.; Kamunde-Devonish, M. K.; Hammann, B. A.; Wills, L. A.; Fullmer, L. B.; Hayes, S. E.; Cheong, P. H. Y.; Casey, W. H.; Nyman, M.; Johnson, D. W. An Overview of Selected Current Approaches to the Characterization of Aqueous Inorganic Clusters. *Dalton Trans.* **2015,** *44*, 16982-17006.

56. Rudolph, W. W.; Pye, C. C. Gallium(III) Hydration in Aqueous Solution of Perchlorate, Nitrate and Sulfate. Raman and 71-Ga NMR Spectroscopic Studies and ab initio Molecular Orbital Calculations of Gallium(III) Water Clusters. *Phys. Chem. Chem. Phys.* **2002,** *4*, 4319-4327.

57. Chen, S.; Hu, C.; Zhang, W.; Chen, J. A Self-Assembling Octahedral Aggregate of Poly(methyl methacrylate) Nanospheres on a Silver Substrate. *ChemPlusChem* **2016,** *81*, 161-165.

58. Demars, T. J.; Bera, M. K.; Seifert, S.; Antonio, M. R.; Ellis, R. J. Revisiting the Solution Structure of Ceric Ammonium Nitrate. *Angew. Chem. Int. Ed.* **2015,** *54*, 7534-7538.

59. Hayez, V.; Costa, V.; Guillaume, J.; Terryn, H.; Hubin, A. Micro Raman Spectroscopy Used for the Study of corrosion products on copper alloys: study of the chemical composition of artificial patinas used for Restoration Purposes. *Analyst* **2005,** *130*, 550-556.

60. Wang, W. W.; Du, P. P.; Zou, S. H.; He, H. Y.; Wang, R. X.; Jin, Z.; Shi, S.; Huang, Y. Y.; Si, R.; Song, Q. S.; Jia, C. J.; Yan, C. H. Highly Dispersed Copper Oxide Clusters as Active Species in Copper-Ceria Catalyst for Preferential Oxidation of Carbon Monoxide. *ACS Catal.* **2015,** *5*, 2088-2099.

61. Si, R.; Raitano, J.; Yi, N.; Zhang, L. H.; Chan, S. W.; Flytzani-Stephanopoulos, M. Structure Sensitivity of the Low-temperature Water-gas Shift Reaction on Cu-CeO_2 Catalysts. *Catal. Today* **2012,** *180*, 68-80.

62. Dziembaj, R.; Molenda, M.; Zaitz, M. M.; Chmielarz, L.; Furczon, K. Correlation of Electrical Properties of Nanometric Copper-doped Ceria Materials ($Ce_{1-x}Cu_xO_{2-\delta}$) with their Catalytic Activity in Incineration of VOCs. *Solid State Ionics* **2013,** *251*, 18-22.

63. Chen, J. F.; Zhan, Y. Y.; Zhu, J. J.; Chen, C. Q.; Lin, X. Y.; Zheng, Q. The Synergetic Mechanism between Copper Species and Ceria in NO Abatement over Cu/CeO2 Catalysts. *Appl. Catal. A-Gen.* **2010,** *377*, 121-127.

64. Konsolakis, M. The Role of Copper-Ceria Interactions in Catalysis Science: Recent Theoretical and Experimental Advances. *Appl. Catal. B-Environ.* **2016,** *198*, 49-66.

65. Campbell, C. T. Catalyst-support Interactions Electronic Pertubations. *Nat. Chem.* **2012,** *4*, 597-598.

66. Senanayake, S. D.; Rodriguez, J. A.; Stacchiola, D. Electronic Metal-Support Interactions and the Production of Hydrogen Through the Water-Gas Shift Reaction and Ethanol Steam Reforming: Fundamental Studies with Well-Defined Model Catalysts. *Top. Catal.* **2013,** *56*, 1488-1498.

67. Guo, R. T.; Zhen, W. L.; Pan, W. G.; Zhou, Y.; Jie-Nan, H.; Xu, H. J.; Jin, Q.; Ding, C. G.; Guo, S. Y. Effect of Cu Doping on the SCR Activity of CeO_2 Catalyst Prepared by Citric Acid Method. *J. Ind. Eng. Chem.* **2014,** *20*, 1577-1580.

68. Ma, L.; Luo, M. F.; Chen, S. Y. Redox Behavior and Catalytic Properties of $CuO/Ce_{0.8}Zr_{0.2}O_2$ Catalysts. *Appl. Catal. A-Gen.* **2003,** *242*, 151-159.